Saito et al. Progress in Earth and Planetary Science (2018) 5:15
https://doi.org/10.1186/s40645-018-0169-6

Progress in Earth and Planetary Science

RESEARCH ARTICLE Open Access

Landslides triggered by an earthquake and heavy rainfalls at Aso volcano, Japan, detected by UAS and SfM-MVS photogrammetry

Hitoshi Saito[1,2*], Shoichiro Uchiyama[3], Yuichi S. Hayakawa[2] and Hiroyuki Obanawa[4]

Abstract

Unmanned aerial systems (UASs) and structure-from-motion multi-view stereo (SfM-MVS) photogrammetry have attracted a tremendous amount of interest for use in the creation of high-definition topographic data for geoscientific studies. By using these techniques, this study examined the topographic characteristics of coseismic landslides triggered by the 2016 Kumamoto earthquake (Mw 7.1) in the Sensuikyo area (1.0 km^2) at Aso volcano, Japan. The study area has frequently experienced rainfall-induced landslide events, such as those in 1990, 2001, and 2012. We obtained orthorectified images and digital surface models (DSMs) with a spatial resolution of 0.06 m before and after the 2016 Kumamoto earthquake. By using these high-definition images and DSMs, we detected a total of 54 coseismic landslides with volumes of 9.1–3994.6 m^3. These landslides, many of which initiated near topographic ridges, were typically located on upside hillslopes of previous rainfall-induced landslide scars that formed in 2012. This result suggests that the topographic effect on seismic waves, i.e., amplification of ground acceleration, was important for coseismic landslide initiation in the study area. The average depth of the coseismic landslides was 1.5 m, which is deeper than the depth of the rainfall-induced landslides prior to these. The total sediment production of the coseismic landslides reached 2.5×10^4 m^3/km^2, which is of the same order as the sediment production triggered by the previous single heavy rainfall event. This result indicates that the effects of the 2016 Kumamoto earthquake in terms of sediment production and topographic changes were similar to those of the rainfall-induced landslide event in the study area.

Keywords: Coseismic landslides, Rainfall-induced landslides, 2016 Kumamoto earthquake, UAS, SfM-MVS photogrammetry, Aso volcano

Introduction

Landslides are major natural hazards that contribute to landscape evolution and erosion in mountainous regions (Keefer and Larsen 2007). Most landslides are triggered by episodic events such as heavy rainfall events, earthquakes, or combinations of both. Differences in location and topographic effects between rainfall-induced landslides and coseismic landslides have been analyzed on the basis of past landslide events (Chang et al. 2007; Meunier et al. 2008). Previous studies have compared rainfall-induced landslides and coseismic landslides in different regions (e.g., Meunier et al. 2008) or rainfall-induced landslides following earthquakes (e.g., Lin et al. 2006).

Japan is characterized by high-relief topography, frequent earthquakes, and rainfall events; thus, rainfall and earthquakes are the dominant triggers of landslides in Japan (e.g., Sato et al. 2005; Saito et al. 2014). In April 2016, the Kumamoto earthquake, which was a series of earthquakes, occurred on Kyushu Island, Japan (Furumura 2016; Lin et al. 2016). The main shock of Mw 7.1 on April 16, which was Mj 7.3 on the Japan Meteorological Agency intensity scale (Fig. 1), caused many landslides near the hypocenter area, including landslides in the Aso volcano region (e.g., Miyabuchi 2016). Among these, several large

* Correspondence: hsaito@kanto-gakuin.ac.jp
[1]College of Economics, Kanto Gakuin University, 1-50-1, Mutsuura-higashi, Kanazawa-ku, Yokohama, Kanagawa 236-8501, Japan
[2]Center for Spatial Information Science, The University of Tokyo, 5-1-5, Kashiwanoha, Kashiwa, Chiba 277-8568, Japan
Full list of author information is available at the end of the article

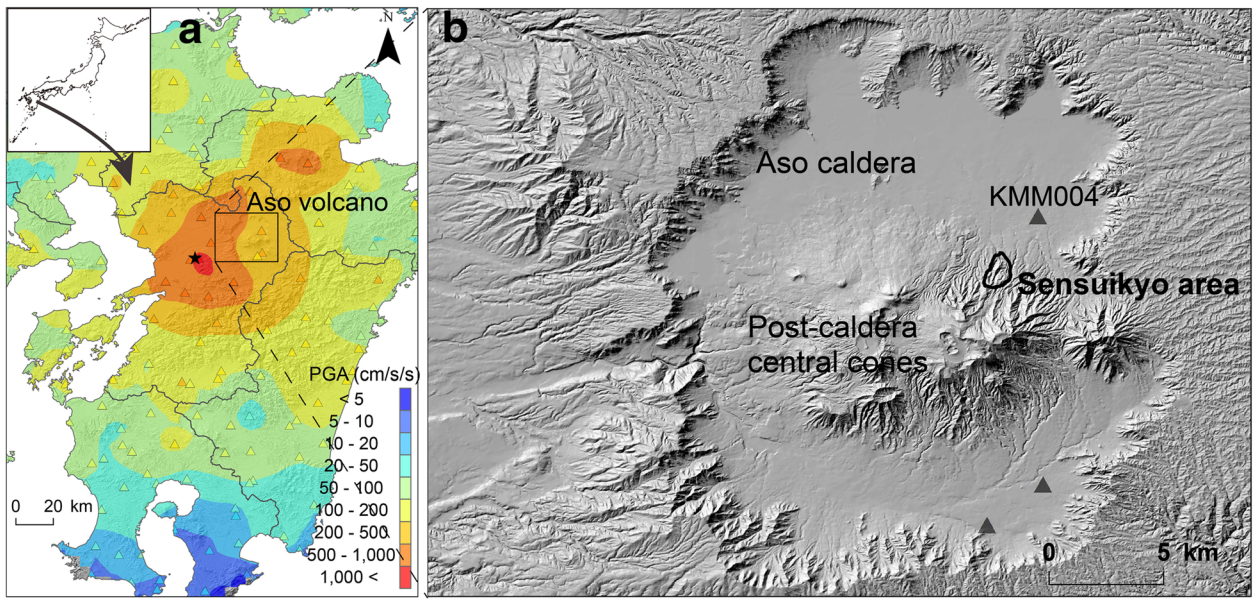

Fig. 1 Study area. **a** Distribution of the peak ground acceleration (PGA; cm/s/s) of the Mw 7.1 main shock of the 2016 Kumamoto earthquake on April 16, derived from records from the K-NET and KiK-net strong motion network (triangles) of the National Research Institute for Earth Science and Disaster Resilience (NIED). The star shows the hypocenter. **b** Aso caldera and location of the Sensuikyo area (black polygon). KMM004 represents the Ichinomiya station of K-NET and KiK-net of NIED

landslides near the hypocenter were detected immediately following the earthquake, and their characteristics and mechanism were analyzed (e.g., Song et al. 2017). However, the 2016 Kumamoto earthquake also caused many smaller landslides with widths of less than a few tens of meters and depths of less than a few meters around the central cones of Aso volcano (Miyabuchi 2016). It is necessary to evaluate the effect of the 2016 Kumamoto earthquake on the overall landslide occurrence, including these smaller landslides. Because landslide size and frequency generally have a nonlinear relationship (Korup et al. 2012), the impact of such smaller landslides in the Aso volcano area remains underestimated.

A limitation on landslide detection from remote sensing images is that landslides due to multiple different events before the time of image shooting cannot be identified from a single image shot at a single point in time (Saito et al. 2009). The Aso volcano region experienced severe rainfall-induced landslide events in 1990, 2001, and 2012 (Miyabuchi and Daimaru 2004; Saito et al. 2016), and the landslide scars from the 2012 event are still obvious in the area. Thus, separating the rainfall-induced landslides from the coseismic landslides caused by the 2016 Kumamoto earthquake in a single image acquired after the earthquake is difficult (Geospatial Information Authority of Japan 2017). Multi-temporal images are required to detect the spatial distributions and topographical characteristics of coseismic and rainfall-induced landslides in the area. Moreover, landslides with smaller volumes are not fully detected in traditional remote sensing images, such as satellite and aerial images, because of the limited spatial resolution. Although light detection and ranging (lidar) data have digital elevation models and aerial images with submeter resolutions (Oguchi et al. 2011), repeating observations by lidar is not cost effective. Recently, unmanned aerial systems (UASs) and structure-from-motion multi-view stereo (SfM-MVS) photogrammetry have become popular methods and have been applied widely in various geomorphological studies (e.g., Westoby et al. 2012). The data processing of SfM-MVS photogrammetry is more straightforward and allows instantaneous acquisition of high-resolution, accurate topographic data from various platforms, including UASs. Unlike satellite images and traditional aerial photographs, the combination of UAS and SfM-MVS photogrammetry provides high-definition orthorectified images and digital surface models (DSMs) for detailed landslide analysis with a spatial resolution of < 1.0 m (Niethammer et al. 2012; Westoby et al. 2012, Hayakawa et al. 2016; James et al. 2017; Peternel et al. 2017). These techniques should enable detection of coseismic and rainfall-induced landslides in the Aso volcano area.

The objective of this study is to examine the spatial distribution and the topographic characteristics of the coseismic landslides triggered by the 2016 Kumamoto earthquake and compare these characteristics with those of the rainfall-induced landslides that occurred in 2012 by using high-definition images and DSMs from UAS and SfM-MVS

photogrammetry. We have conducted field monitoring using UAS at the northern part of the central cones of Aso volcano since 2012 to measure rainfall-induced landslides (Saito et al. 2016). The study area is suitable for comparing coseismic landslides with rainfall-induced landslides. Additionally, landslide susceptibility may have increased because of a decrease in slope stability caused by earthquakes (Jan and Chen 2005; Lin et al. 2006; Chang et al. 2007). Detailed geomorphological and spatial-statistical studies on the characteristics of the landslides triggered by the 2016 Kumamoto earthquake are therefore needed to assess future landslide hazards.

Study area

Aso volcano is composed of Aso caldera and post-caldera central cones (Fig. 1). The Aso caldera, running 25 km north–south and 18 km east–west, was formed by four gigantic pyroclastic-flow eruptions of andesitic to rhyolitic magma from about 270 to 90 ka (Ono et al. 1977; Miyabuchi and Daimaru 2004). The post-caldera central cones were formed soon after the last caldera-forming eruption at 90 ka and have produced large volumes of fallout tephra and lava flows. At least 17 cones are visible on the surface (Miyabuchi 2009).

This study analyzed the Sensuikyo area (1.0 km^2, Fig. 1b) located at the northern slopes of the post-caldera central cones, where many landslides were triggered by both the 2016 Kumamoto earthquake and the heavy rainfall events of 1990, 2001, and 2012. These slopes steepen with elevation. The elevation in the study area ranges from about 620 to 860 m, the angle of the hillslopes ranges from about 25° to 45°, and the angle of the channel slopes is < 15°. The study area is characterized by grass vegetation used for grazing, which is the typical landscape of the Aso volcano region (Fig. 2). Several deciduous trees are distributed along the channels.

The study area is located downwind of the prevailing direction of tephra dispersal from the active post-caldera central cones. Volcanic ash and lapilli with a thickness of 10 m or more have accumulated there during the Holocene (Miyabuchi and Watanabe 1997). The thick tephra layers are composed mostly of sand- to silt-size ash-fall deposits and several scoria-fall deposits, which are interbedded with humic paleosols (Miyabuchi 2009).

The distribution of the peak ground acceleration (PGA) of the Mw 7.1 main shock of the 2016 Kumamoto earthquake is shown in Fig. 1a. Strong ground motion spread throughout Kyushu Island. In particular, large PGA

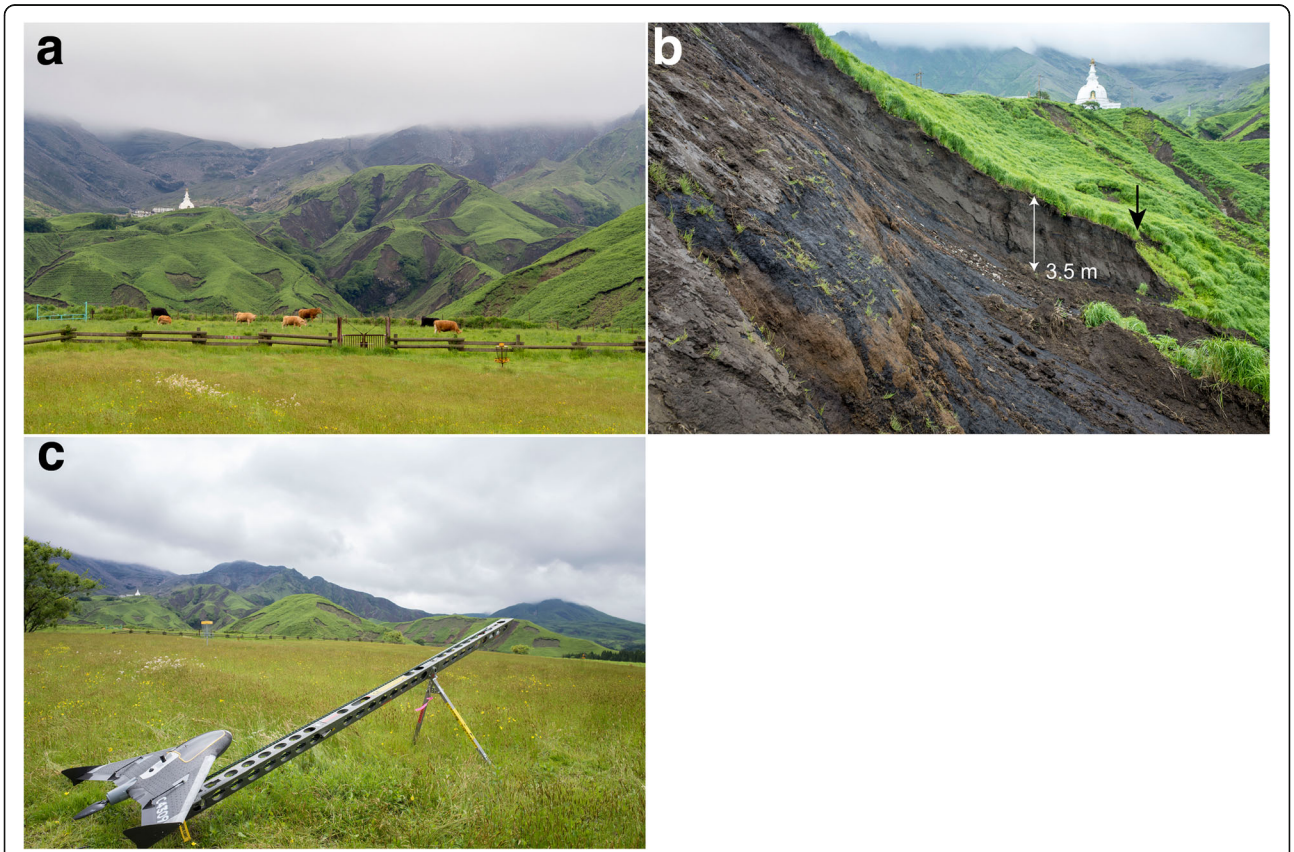

Fig. 2 Sensuikyo area following the 2016 Kumamoto earthquake. **a** Overview of the study area, **b** coseismic landslide scar and rainfall-induced landslide scarps (black arrow) described in Fig. 4, and **c** the investigation using Trimble UX5

contours of > 200 cm/s/s extend from the hypocenter toward the northeast region along the fault zone (Furumura 2016). The study area is 31 km northeast of the hypocenter. Ichinomiya station (KMM004 in Fig. 1b) observed a PGA of 403 cm/s/s. The effect of the significant shaking of the main shock on the surface soils caused landslides characterized by shallow slides with a depth of a few meters (Fig. 2b).

The study area experienced frequent severe landslide events triggered by heavy rainfalls in July 1990, June 2001, and July 2012 (Miyabuchi and Daimaru 2004; Saito et al. 2016). The stratified composition of the thick tephra affected the hydrological characteristics of the slopes of the study area and controlled the rainfall-induced landslides (Miyabuchi and Daimaru 2004; Shimizu and Ono 2016). Most of these landslides were shallow in unconsolidated tephra deposits at depths of < 1.0 m. In July 2012, a heavy rainfall event of 85.0 and 427.6 mm for maximums of 1 and 24 h rainfalls, respectively, triggered many shallow landslides. We conducted a field survey with a UAS to detect the location of these landslides in 2014. The heavy rainfall in 2012 caused 378 shallow landslides with an average depth of 0.7 m in the study area (Saito et al. 2016).

Methods/experimental

We conducted field surveys on March 17 and May 11, 2016, before and after the 2016 Kumamoto earthquake, respectively. Aerial imageries of the study area were obtained by using the UAS (Trimble UX5) with a digital camera (SONY NEX-5T, 16.10 megapixels) (Table 1, Fig. 2c), which enabled autonomous flight and image acquisition. Images were captured at an altitude of about 140 m above ground level with 80% overlap and 80% sidelap. In total, more than 1000 images were acquired in March and May 2016. The theoretical spatial resolution of the images was 0.04 m. We measured ground control points (GCPs) using a global navigation satellite system (GNSS; Trimble GeoExplorer 6000XH) by the kinematic method (Table 1).

Table 1 General information related to the unmanned aerial system (UAS), camera, and global navigation satellite system (GNSS)

UAS	
Airplane model	Trimble UX5
Airplane type	Fixed-wing aircraft
Weight	2500 g
Max. duration of flight	50 min
Cameras	
Camera model	SONY NEX-5 T
Number of pixels	16.10 M
Sensor size	23.6 × 15.6 mm
Focal length	15 mm
GNSS	
Receiver	Trimble GeoExplorer 6000XH
Antenna	Trimble Zephyr Geodetic 2
Frequency band	GPS L1/L2, GLONASS L1/L2, SBAS

These aerial images were processed with 10 GCPs by using SfM-MVS photogrammetry software (Agisoft PhotoScan, professional version). Following the standard SfM-MVS photogrammetry workflow, we obtained orthorectified images and DSMs. Because the study area was covered by grass vegetation in May 2016, the DSMs include grass height, except at landslide scars (Fig. 2b). However, the grass is burned off for grazing in the early spring, from late February to early March of each year. We acquired the first set of aerial images just after the burning in March 2016. Therefore, the DSM acquired in March can be regarded as a digital terrain model (DTM) of the area. These processes used to create the orthorectified images and DSMs were verified by Saito et al. (2016). The spatial accuracy as the root mean square error (RMSE) of these data was 0.08 and 0.09 m in the horizontal and vertical directions, respectively.

This study compared the orthorectified images and DSMs acquired in March and May 2016 to detect landslides. To avoid the effect of the crustal deformation triggered by the 2016 earthquake, the orthorectified image and DSM in May 2016 were co-registered to the geographic coordinates of the orthorectified image and DSM in March 2016. Sequential DSMs with the same spatial resolution were used to create a difference of DSMs based on cell-by-cell subtraction. Such sequential DSMs are particularly relevant to geomorphic studies because a difference of DSMs provides a high-resolution, spatially distributed surface model of the topographic and volumetric changes through time (e.g., James et al. 2012). The DSM that was acquired in May 2016 included vegetation height, but the landslide scars had no vegetation. We confirmed that no new landslide events, other than those triggered by the earthquake, were observed between March and May 2016. The difference of DSMs in landslide scars therefore showed topographic changes caused by landslides triggered by the 2016 Kumamoto earthquake, allowing us to obtain landslides volumes.

We then detected initiation areas of coseismic landslides larger than 10.0 m^2 by using the orthorectified images and the difference of DSMs. Although separation of landslide initiation, transport, and deposition areas from orthorectified images alone was difficult, we detected

landslide initiation areas from the decreased areas in the difference of DSMs. We calculated the area and volume of each landslide from the orthorectified images and the difference of DSMs. The total sediment production of the coseismic landslides was estimated from the net changes in topography.

The distribution of rainfall-induced landslides in 2012 was provided by Saito et al. (2016), who also detected landslide initiation areas using orthorectified images and a difference of DSMs obtained by UAS and SfM-MVS photogrammetry. We compared the distribution and topographic characteristics of the landslides triggered by the heavy rainfall in 2012 with those of the landslides triggered by the 2016 Kumamoto earthquake.

This study examined the topographic locations of these coseismic and rainfall-induced landslides in terms of distances from ridge and stream networks, which were derived from the DSMs. We calculated the distance from the center cell of a landslide initiation area to the nearest ridge (d_{ridge}) and the distance to the nearest stream (d_{stream}). The distance to the nearest ridge was normalized by the total length of the measured landslide hillslope using

$$|d_{\mathrm{ridge}}| = \frac{d_{\mathrm{ridge}}}{d_{\mathrm{ridge}} + d_{\mathrm{stream}}}. \quad (1)$$

$|d_{\mathrm{ridge}}|$ varies from 0 for a cell located in a ridge to 1 for a stream cell. This normalized distance can be used to examine the relative positions of coseismic and rainfall-induced landslides on the hillslopes.

Results

We obtained orthorectified images and DSMs with spatial resolutions of 0.06 m in March and May 2016 (Fig. 3). A comparison of these images and DSMs between the 2 months revealed that 54 landslides and many fissures occurred near topographic ridges in the study area as a result of the 2016 Kumamoto earthquake (Figs. 3, 4, and 5). The area of the coseismic landslides ranged from 11.3 to 1461.2 m^2, and the total area of the landslides reached 1.2×10^4 m^2, which corresponds to 1.2% of the study area.

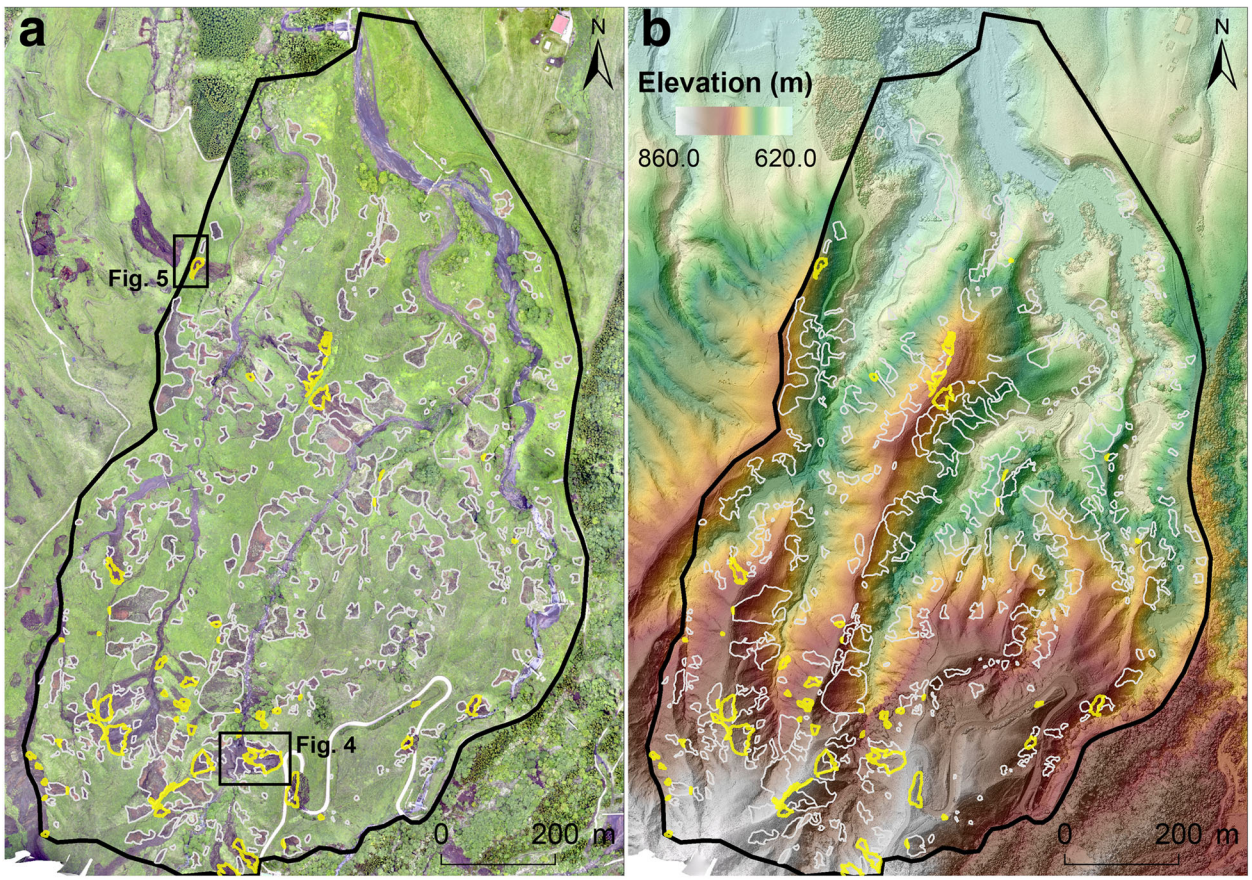

Fig. 3 Distributions of landslide initiation areas triggered by the 2016 Kumamoto earthquake (yellow polygons) and the heavy rainfalls of 2012 (white polygons) with the **a** orthorectified images and **b** digital surface models (DSMs), with a spatial resolution of 0.06 m, acquired in May 2016. The black polygon shows the study area. Details in the black rectangles are shown in Figs. 4 and 5, respectively

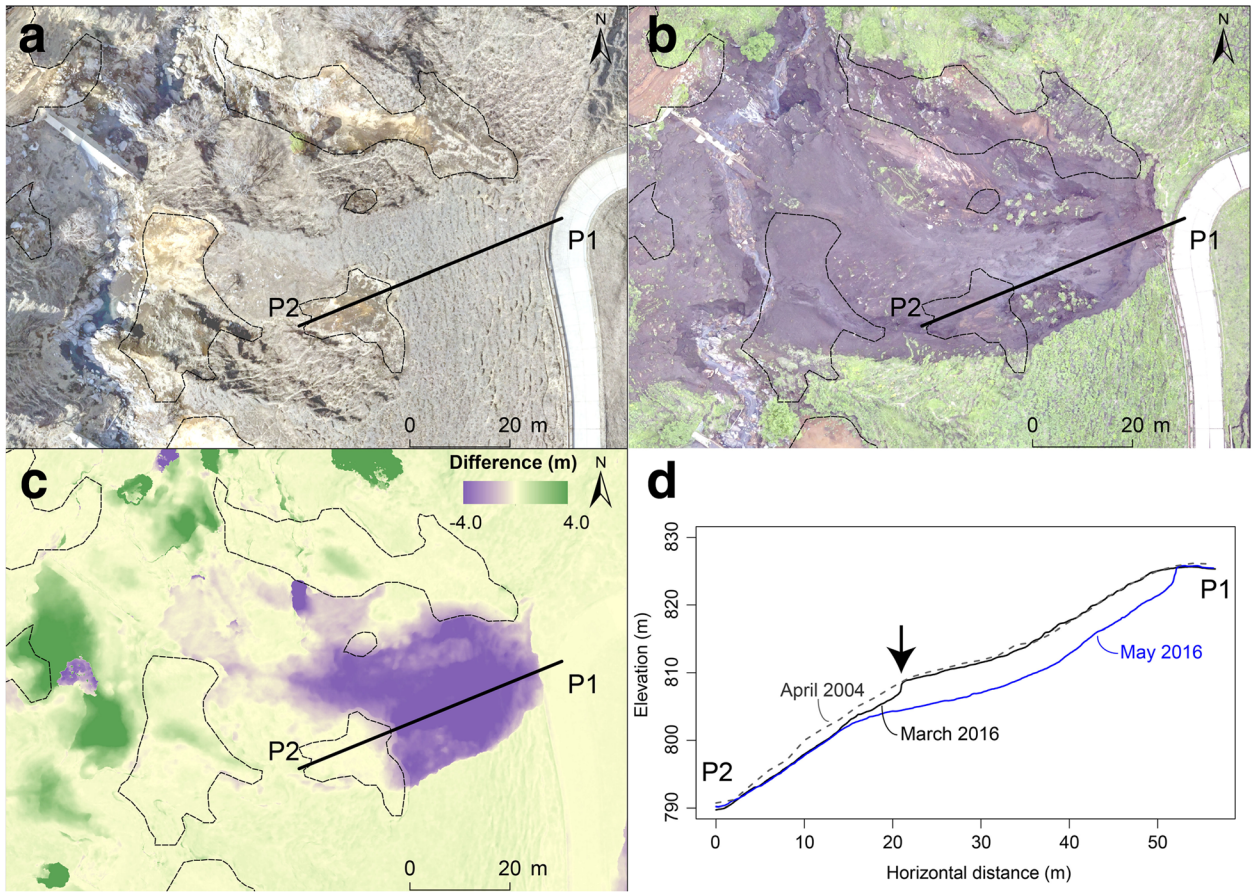

Fig. 4 Examples of landslides triggered by the heavy rainfalls of 2012 (black polygons) and the 2016 Kumamoto earthquake (shown in **b**) on orthorectified images acquired in **a** March 2016 and **b** May 2016. **c** Difference of digital surface models (DSMs) between March and May 2016 (blue represents a decrease in DSM). **d** Profile of the slope on which the landslide was located in April 2004 (gray dashed line), March 2016 (black line), and May 2016 (blue line), shown by the black profile line (P1–P2). The arrow in **d** shows the scarp of the rainfall-induced landslide in 2012. The slope profile in April 2004 was derived from lidar-based DSM with a spatial resolution of 2.0 m (Saito et al. 2016)

Figure 6 shows the difference of DSMs between May and March. Most of the area is characterized by increases in DSM (higher in May than in March) that represent sedimentation of landslides along channels, growth of grass, and leafing of deciduous trees between March and May. Areas of decrease represent erosion areas caused by landslides. The depth of coseismic landslides ranged from 0.8 to 4.6 m, with an average of 1.5 m. Individual landslide volume, estimated from the difference of DSMs, ranged from 9.1 to 3994.6 m^3 with an average of 458.3 m^3. The total sediment production reached 2.5×10^4 m^3/km^2.

The distribution of the coseismic landslides was not uniform (Figs. 3 and 6). The landslides initiated near topographic ridges of steep and high-relief slopes (Fig. 7). Because the slopes become steeper with elevation in the southern part of the study area, the landslides were clustered there. Figure 3 also shows the distribution of the rainfall-induced landslides of 2012, which had a total of 378 sites and an average depth of 0.7 m. The rainfall-induced landslides were distributed over all slope segments but were clustered in the lower parts of the hillslopes (Fig. 7).

A comparison of the initiation areas of the landslides triggered by rainfall and by the earthquake revealed that the coseismic landslides initiated in the upper parts of hillslopes of rainfall-induced landslide scars in the study area (Figs. 3 and 7). Eighteen coseismic landslides with volumes < 100.0 m^3 around rainfall-induced landslide scarps were shallow failures with depths < 1.0 m. However, 36 landslides had depths > 1.0 m, which is larger than the depth of the rainfall-induced landslides (Fig. 4). The coseismic landslides in the area were characterized by deep slip surfaces, and they occurred in the upside slope of the previous rainfall-induced landslide scar in the area.

Discussion

Earthquakes trigger landslides because the combination of gravitational and seismic acceleration causes the short-

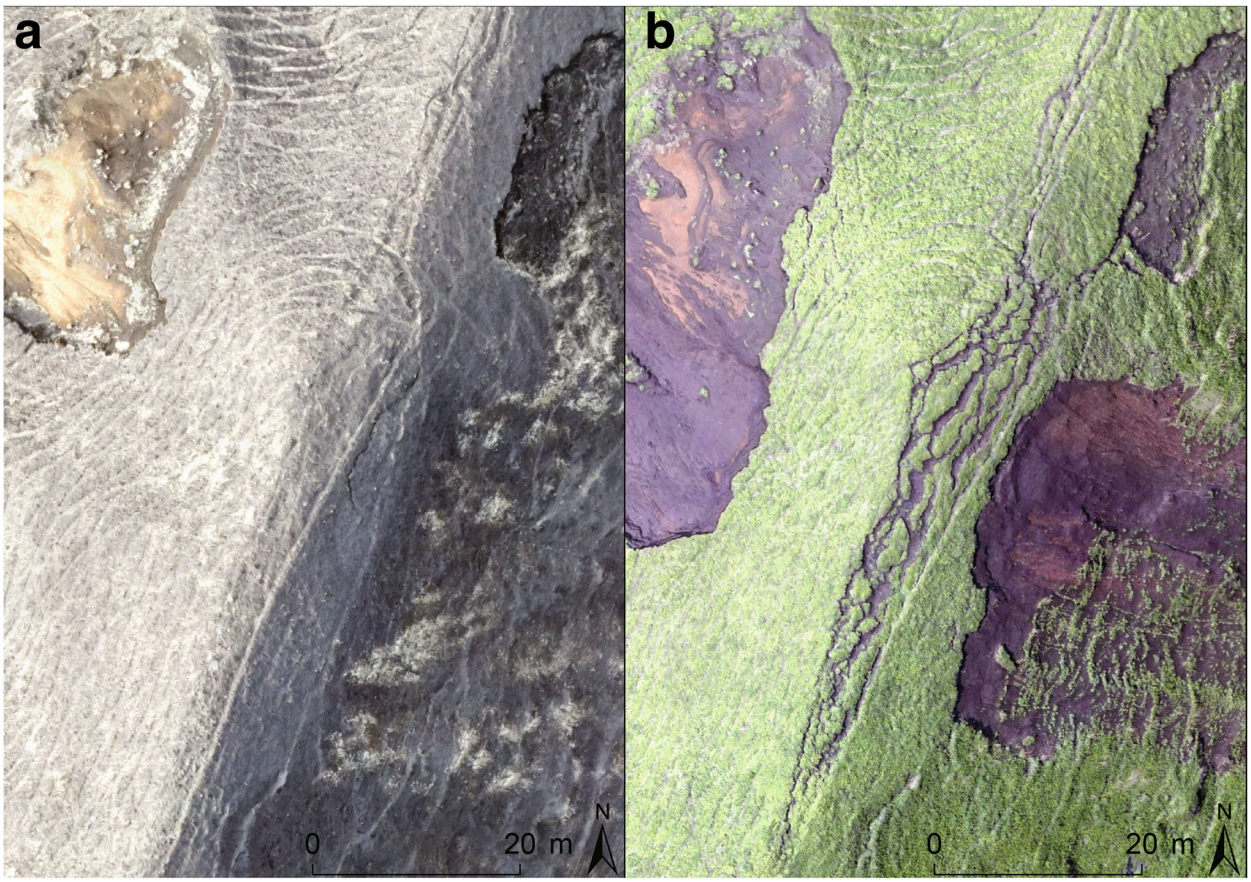

Fig. 5 Example of fissures triggered by the 2016 Kumamoto earthquake shown by orthorectified images acquired in **a** March and **b** May 2016

lived stress to be greater than the combined cohesive and frictional strength of the underlying rocks and soils (e.g., Newmark 1965). The topographic characteristics of the locations of coseismic landslides have been discussed for past earthquake events in mountainous regions. For example, observation of coseismic landslides and modeling of seismic waves have shown that these landslides tend to cluster near ridge crests, where landslide susceptibility is highest (Chang et al. 2007; Meunier et al. 2008). The present study also showed that the 2016 Kumamoto earthquake triggered landslides near topographic ridges in the area (Fig. 7).

In contrast, the rainfall-induced landslides of 2012 were distributed throughout the slope segment, but were clustered in the lower hillslopes (Fig. 7). Fifty-four percent of the landslides initiated in the lower half of hillslopes and at the convex-up knicklines of the hillslopes (Figs. 4 and 7). Our results showed that the coseismic landslides initiated at upside hillslopes of previous rainfall-induced landslide scars in the study area. During an earthquake, ground accelerations are amplified in both topographic ridges and convex-up knicklines within ridge flanks (Meunier et al. 2008). The landslide rate decreases systematically with distance from the earthquake hypocenter as the seismic waves spread and attenuate, and the topographic site effects on the seismic waves dominate the landslide pattern on the scale of an individual mountain ridge (Meunier et al. 2007). The study area is located about 31 km from the hypocenter. However, the area is characterized by high relief and steep hillslopes. Hence, the topographic site effects on the seismic waves were important for amplification of ground acceleration and for landslide initiation. Our results suggest that erosion caused by past rainfall-induced landslides in the lower hillslopes decreased the slope stability at the upper hillslopes, which made these hillslopes susceptible to coseismic landsliding.

The depth of coseismic landslides was larger than the depth of the rainfall-induced landslides. The stratified composition of the thick tephra in the hillslopes affected the hydrological characteristics of the slopes in the study area and controlled the rainfall-induced landslides (Miyabuchi and Daimaru 2004; Shimizu and Ono 2016). The slip surface of the rainfall-induced landslides was formed near the boundary between upper blackish and lower brownish tephra layers; the horizon is dated as

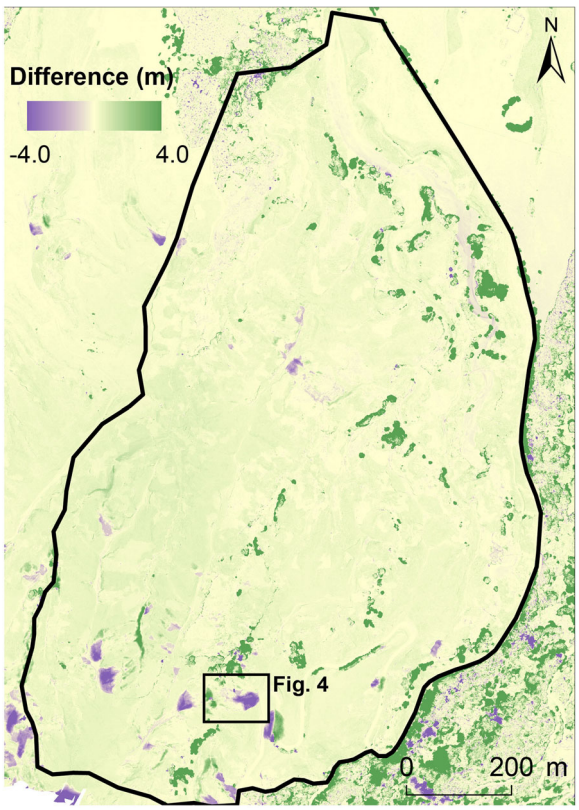

Fig. 6 Difference of digital surface models (DSMs) between May and March 2016. Blue represents a decrease in DSM caused by coseismic landslides, whereas green represents sedimentation of landslides along channels, increased grass growth, or leafing of deciduous trees. Details in the black rectangle are shown in Fig. 4. The black polygon shows the study area

3000 years old (Miyabuchi and Daimaru 2004). These features were detected for the rainfall-induced landslides in 2012, when the landslide depth was generally < 1.0 m, with an average of 0.7 m in the study area (Saito et al. 2016). However, the present study showed that the coseismic landslides had depths reaching > 3.0 m, with an average of 1.5 m. These results indicate that the potential slip surfaces of the coseismic landslides were different from those of the rainfall-induced landslides.

Our results show that the total sediment production owing to the coseismic landslides reached 2.5×10^4 m^3/km^2. The study area has frequently experienced severe landslide events triggered by heavy rainfalls in the past three decades (Miyabuchi and Daimaru 2004; Saito et al. 2016). A statistical analysis of the probable rainfall showed that these landslide events were likely triggered by rainfall events with return periods shorter than about 20 years (Table 2). The sediment production and discharge triggered by a single heavy rainfall event was estimated to be from 10^3 to 10^5 m^3/km^2, which corresponds to the sediment production triggered by the 2016 Kumamoto earthquake (Table 2). Although the total number of coseismic landslides was smaller than that of rainfall-induced landslides, the coseismic landslide depth was larger than the rainfall-induced landslide depth. The total effect of the 2016 Kumamoto earthquake on the sediment production and topographic change had a similar impact as a single heavy rainfall-induced landslide event in the study area.

Previous studies have shown that earthquakes strongly influenced the locations and susceptibility of subsequent rainfall-induced landslides (Lin et al. 2006; Chang et al. 2007; Tang et al. 2011). The 2005 Kashmir earthquake caused extensive fissures which could potentially cause additional landslides (Owen et al. 2008). Our orthorectified images and DSMs also showed many fissures near

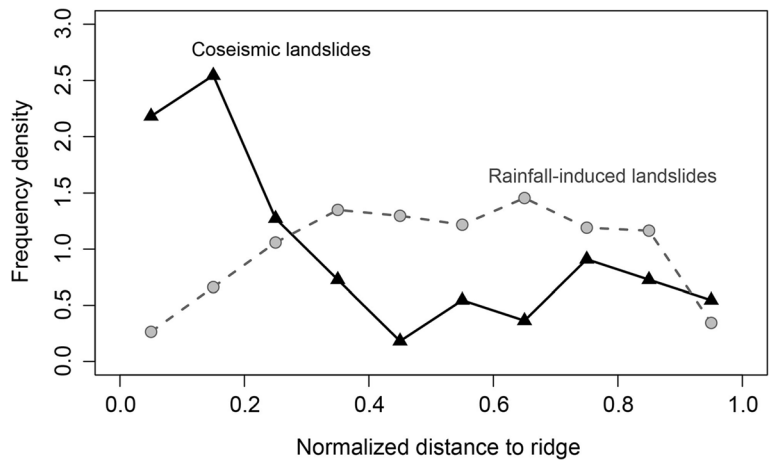

Fig. 7 Frequency density distributions of normalized distances to ridges from coseismic (black line) and rainfall-induced (gray dashed line) landslides. Normalized distances to ridges vary from 0 for a cell located on the ridge to 1 for a stream cell

Table 2 Comparison of sediment discharge and production triggered by the heavy rainfall events in 1990, 2001, and 2012 (after Miyabuchi and Daimaru, 2004 and Saito et al. 2016), and the 2016 Kumamoto earthquake. The rainfalls and return periods were calculated from radar/rain-gauge analyzed precipitation provided by the Japan Meteorological Agency (Saito and Matsuyama, 2015)

Event	July 1990	June 2001	July 2012	2016 Kumamoto earthquake
Max. 1 h rainfall/return period	80.0 mm/12 years	90.0 mm/23 years	85.0 mm/16 years	0.0 mm
Max. 24 h rainfall/return period	497.8 mm/26 years	297.0 mm/2 years	427.6 mm/11 years	0.0 mm
Sediment discharge (sediment production, m^3/km^2)	$3.1–3.9 \times 10^4$	$3.0–4.1 \times 10^3$	$1.2–4.8 \times 10^5$	2.5×10^4

topographic ridges (Fig. 5). These facts imply that the 2016 Kumamoto earthquake influenced the stability of the hillslopes and that future landslide development may occur with lower-frequency rainfall events. Future studies are necessary to track these fissures and evaluate subsequent rainfall-induced landslides.

Conclusions

By using the advantages of the high-definition data, repeatability, and mobility provided by the UAS and the SfM-MVS photogrammetry method, this study detected the distribution of landslides triggered by the 2016 Kumamoto earthquake. We analyzed the Sensuikyo area at the northern slope of Aso volcano, where rainfall-induced landslide events have been frequent during the past three decades.

We obtained orthorectified images and DSMs with a spatial resolution of 0.06 m. By determining the differences between the data obtained in March and May 2016, which correspond to times before and after the earthquake, respectively, we detected 54 coseismic landslides with volumes ranging from 9.1 to 3994.6 m^3. These landslides initiated near topographic ridges characterized by upside hillslopes of past rainfall-induced landslide scars. Topographic site effects on seismic waves, i.e., amplification of ground acceleration, were important for the landslide initiation in the study area. Our results suggest that erosion caused by the previous rainfall-induced landslides decreased slope stability, which made the hillslopes susceptible to coseismic landsliding.

The depth of the coseismic landslides reached > 3.0 m, with an average of 1.5 m, which is larger than the rainfall-induced landslide depth. The total sediment production owing to coseismic landslides was 2.5×10^4 m^3/km^2, which is of the same order as the sediment production triggered by a single heavy rainfall event. These results indicate that the effects of the 2016 Kumamoto earthquake on the sediment production and topographic changes had a similar impact as a rainfall-induced landslide event.

Abbreviations

DSM: Digital surface model; DTM: Digital terrain model; GNSS: Global Navigation Satellite System; PGA: Peak ground acceleration; SfM-MVS: Structure-from-motion multi-view stereo; UAS: Unmanned aerial system

Acknowledgements

We thank Dr. Yasufumi Iryu, Dr. Jun Matsumoto, Dr. Shigekazu Kusumoto, and two anonymous reviewers for their helpful comments that improved the manuscript. This study was supported by KAKENHI Grant Numbers JP15K16287, JP17915136, JP25702014, and JP17H02031, and joint research with CSIS, The University of Tokyo (No. 554). We computed statistics using the R software environment (http://www.r-project.org/).

Funding

This work was supported by JSPS KAKENHI Grant Numbers JP15K16287, JP17915136, JP25702014, and JP17H02031.

Availability of data and materials

The data used in this paper are available from the authors on request.

Authors' contributions

HS proposed the topic, conceived and designed the study. SU, YH, and HO carried out the field measurements and collaborated with the corresponding author in the construction of the manuscript. All authors read and approved the final manuscript.

Competing interests

The authors declare that they have no competing interests.

Publisher's Note

Author details

[1]College of Economics, Kanto Gakuin University, 1-50-1, Mutsuura-higashi, Kanazawa-ku, Yokohama, Kanagawa 236-8501, Japan. [2]Center for Spatial Information Science, The University of Tokyo, 5-1-5, Kashiwanoha, Kashiwa, Chiba 277-8568, Japan. [3]National Research Institute for Earth Science and Disaster Resilience, 3-1, Ten-nodai, Tsukuba, Ibaraki 305-0006, Japan. [4]VisionTech Inc., 2-1-16 Umezono, Tsukuba, Ibaraki 305-0045, Japan.

Received: 29 June 2017 Accepted: 1 February 2018
Published online: 01 March 2018

References

Chang KT, Chiang SH, Hsu ML (2007) Modeling typhoon- and earthquake-induced landslides in a mountainous watershed using logistic regression. Geomorphology 89:335–347

Furumura T (2016) Destructive near-fault strong ground motion from the 2016 Kumamoto prefecture, Japan, M7. 3 earthquake. Landslides 13:1519–1524

Geospatial Information Authority of Japan (2017) Landslide inventory maps triggered by the 2016 Kumamoto earthquake. Available via http://www.gsi.go.jp/BOUSAI/H27-kumamoto-earthquake-index.html (in Japanese). Accessed 17 June 2017

Hayakawa YS, Obanawa H, Saito H, Uchiyama S (2016) Geomorphological applications of structure-from-motion multi-view stereo photogrammetry: a review. Transactions, Japanese Geomorphological Union 37:1–30 (in Japanese with English abstract)

James LA, Hodgson ME, Ghoshal S, Latiolais MM (2012) Geomorphic change detection using historic maps and DEM differencing: the temporal dimension of geospatial analysis. Geomorphology 137:181–198

James MR, Robson S, d'Oleire-Oltmanns S, Niethammer U (2017) Optimising UAV topographic surveys processed with structure-from-motion: ground control quality, quantity and bundle adjustment. Geomorphology 280:51–66

Jan CD, Chen CL (2005) Debris flows caused by typhoon herb in Taiwan. In: Jakob M, Hungr O (eds) Debris flow hazards and related phenomena. Springer, Berlin Heidelberg, pp 539–563. https://doi.org/10.1007/3-540-27129-5_21
Keefer DK, Larsen MC (2007) Assessing landslide hazards. Science 316:1136–1138. https://doi.org/10.1126/science.1143308
Korup O, Görüm T, Hayakawa YS (2012) Without power? Landslide inventories in the face of climate change. Earth Surf Process Landf 37:92–99
Lin A, Satsukawa T, Wang M, Asl ZM, Fueta R, Nakajima F (2016) Coseismic rupturing stopped by Aso volcano during the 2016 mw 7.1 Kumamoto earthquake, Japan. Science 354(6314):869–874
Lin CW, Liu SH, Lee SY, Liu CC (2006) Impacts of the chi-chi earthquake on subsequent rainfall-induced landslides in central Taiwan. Eng Geol 86:87–101
Meunier P, Hovius N, Haines JA (2007) Regional patterns of earthquake-triggered landslides and their relation to ground motion. Geophys Res Lett 34:L20408. https://doi.org/10.1029/2007GL031337
Meunier P, Hovius N, Haines JA (2008) Topographic site effects and the location of earthquake-induced landslides. Earth Planet Sci Lett 275(3):221–232
Miyabuchi Y (2009) A 90,000-year tephrostratigraphic framework of Aso volcano, Japan. Sediment Geol 220:169–189
Miyabuchi Y (2016) Landslide disaster triggered by the 2016 Kumamoto earthquake in and around Minamiaso village, western part of Aso caldera, southwestern Japan. J Geogr (Chigaku Zasshi) 125:421–429 (in Japanse with English abstract)
Miyabuchi Y, Daimaru H (2004) The June 2001 rainfall-induced landslides and associated lahars at Aso volcano (southwestern Japan): implications for hazard assessment. Acta Vulcanol 16:21–36
Miyabuchi Y, Watanabe K (1997) Eruption ages of Holocene tephras from Aso volcano, southern Japan, inferred from 14C ages of buried andisols. Bulletin of the Volcanological Society of Japan 42:403–408 (in Japanese with English abstract)
Newmark NM (1965) Effects of earthquakes on dams and embankments. Geotechnique 15(2):139–160
Niethammer U, James MR, Rothmund S, Travelletti J, Joswig M (2012) UAV-based remote sensing of the super-Sauze landslide: evaluation and results. Eng Geol 128:2–11. https://doi.org/10.1016/j.enggeo.2011.03.012
Oguchi T, Hayakawa YS, Wasklewicz T (2011) Data sources. In: Smith MJ, Paron P, Griffiths JS (eds) Developments in earth surface processes: geomorphological mapping: methods and applications. Elsevier, pp 189–224
Ono K, Matsumoto Y, Miyahisa M, Teraoka Y, Kambe N (1977) Geology of the Taketa district. Geological Survey of Japan, p 145 (in Japanse with English abstract)
Owen L, Kamp U, Khattak GA, Harp E, Keefer D, Bauer MA (2008) Landslides triggered by the 8 October 2005 Kashmir earthquake. Geomorphology 94:1–9
Peternel T, Kumelj Š, Oštir K, Komac M (2017) Monitoring the Potoška planina landslide (NW Slovenia) using UAV photogrammetry and tachymetric measurements. Landslides 14:395–406
Saito H, Korup O, Uchida T, Hayashi S, Oguchi T (2014) Rainfall conditions, typhoon frequency, and contemporary landslide erosion in Japan. Geology 42:999–1002
Saito H, Matsuyama H (2015) Probable hourly precipitation and soil water index for 50-yr recurrence interval over the Japanese archipelago. Science Online Letters on the Atmosphere 11:118–123
Saito H, Nakayama D, Matsuyama H (2009) Comparison of landslide susceptibility based on a decision-tree model and actual landslide occurrence: the Akaishi Mountains, Japan. Geomorphology 109:108–121
Saito H, Uchiyama S, Obanawa H, Hayakawa YS (2016) Sediment yields triggered by heavy rainfall in July 2012 at Aso volcano: application of high-definition topography data using unmanned aerial vehicles and structure-from-motion multi-view stereo photogrammetry. Geographical Review of Japan Series A 89:347–359 (in Japanese with English abstract)
Sato HP, Sekiguchi T, Kojiroi R, Suzuki Y, Iida M (2005) Overlaying landslides distribution on the earthquake source, geological and topographical data: the mid Niigata prefecture earthquake in 2004, Japan. Landslides 2(2):143–152
Shimizu O, Ono M (2016) Relationship of tephra stratigraphy and hydraulic conductivity with slide depth in rainfall-induced shallow landslides in Aso volcano, Japan. Landslides 13:577–582
Song K, Wang F, Dai Z, Iio A, Osaka O, Sakata S (2017) Geological characteristics of landslides triggered by the 2016 Kumamoto earthquake in Mt. Aso volcano, Japan. Bull Eng Geol Environ:1–10
Tang C, Zhu J, Qi X, Ding J (2011) Landslides induced by the Wenchuan earthquake and the subsequent strong rainfall event: a case study in the Beichuan area of China. Eng Geol 122(1):22–33
Westoby MJ, Brasington J, Glasser NF, Hambrey MJ, Reynolds JM (2012) 'Structure-from-motion' photogrammetry: a low-cost, effective tool for geoscience applications. Geomorphology 179:300–314